

Saturation Effects in High Acceleration Bearingless Motors

P. Karutz*, T. Nussbaumer**, W. Gruber*** and J.W. Kolar*

* ETH Zurich, Power Electronic Systems Laboratory, 8092 Zurich, Switzerland, karutz@lem.ee.ethz.ch

** Levitronix GmbH, Technoparkstrasse 1, 8005 Zurich, Switzerland

*** ACCM GmbH (Johannes Kepler Universität Linz), Altenbergerstr. 69, 4040 Linz, Austria

Abstract – Bearingless motors offer contactless levitation and rotation through a hermitically closed process chamber and satisfy the increasing demand for ultra high purity spin processes in chemical, biochemical and semiconductor industry. Most of these processes require a high acceleration capability for minimal process times and a large air gap in order to fit in a mechanical stable chamber wall. The combination of these requirements possibly causes saturation effect issues that may occur depending on the specific drive claw shape. In this paper, saturation effects which reduce the effective torque of the motor are investigated for two commonly known drive claw shapes. The investigations are exemplarily carried out for the Bearingless 2-Level Motor (B2M), since it allows the isolated examination of saturation effects caused by the drive flux due to the axial and circumferential separation of the bearing and drive units. The paper visualizes the flux density distribution and the flux trajectory change at the presence of saturation for the presented drive claw shapes by means of 3D finite element simulations. One drive claw type is found to be the more applicable concept and is subsequently optimized with respect to maximum torque by variation of the drive claw width. Finally, the superior performance of the designed claw is proven by the comparison of simulation results with measurement data of an experimental prototype.

I. INTRODUCTION

Several different concepts for high acceleration bearingless motors have been introduced in the past [1] – [4]. In particular, bearingless slice motors have the advantage of a low profile height due to the passive stabilization of the tilting and axial displacement [5]. Therefore they can be implemented with a high level of compactness. The rotor of these motors is levitated contactless by magnetic forces through an air gap, giving the possibility to encapsulate the rotor and separate it from the motor stator through a process chamber. At the inside of the process chamber a hermetically closed and ultra-clean room with process dependent conditions (specific pressure, temperature, humidity) can be locally generated. Application fields of high interest for this kind of setup are found in the pharmaceutical, chemical, biochemical and semiconductor industry, where wearless and lubrication free spin processes are usually required.

Taking the field of application into consideration, three main requirements for the introduced motors can be defined. First, a large air gap is required in order to ensure a minimum process chamber wall thickness and therefore its mechanical robustness. Secondly, a high torque capability, resulting in a high acceleration capability, is desired in order to minimize the times between process rotation speeds consequently reducing the equipments operating costs. And last, the process defined

maximum rotational speed has to be reached, while ensuring a stable and vibration-free operation.

A motor concept that combines the before mentioned requirements is the “Bearingless 2-Level Motor (B2M)” that was introduced in [4]. It will be used as an exemplary design in the following since its axially and circumferential separated bearing and drive claws allow a better isolated view on occurring effects in the stator drive claws. However, the following design considerations can be adapted to the other before-mentioned bearingless motor concepts. Especially for [2] and [3], the superposition of the bearing and drive fluxes in the stator claws has to be taken into account.

In Fig. 1 a top view of the B2M is depicted. Here, the magnetic bearing and the permanent magnet synchronous drive are separated on different circumferential positions and axial levels. Due to the limited circumferential space that has to be split between the bearing and drive and the demand for an axially compact design, the drive is implemented using concentrated windings. As compared to drives with full circumferential drive claw placement, concentrated windings tend to cause higher flux densities in their drive claw cross sections due to the higher ampere-turn ratio. As a consequence, saturation effects may occur in the claws, which then dramatically lower the effective drive torque as will be shown in this paper. The topic of saturation effects in bearingless motors is of special interest as discussed in [6] and needs detailed investigation for

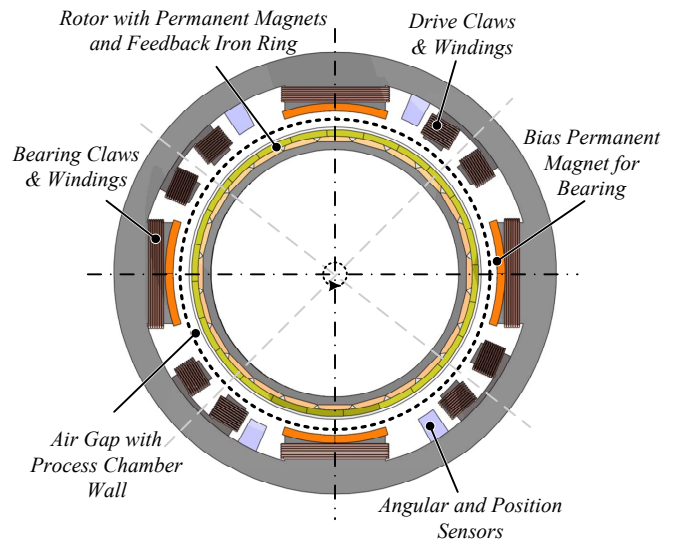


Fig. 1: Top view on the “Bearingless 2-Level Motor (B2M)” showing the circumferential space distribution for the bearing and drive coils.

the design of a high acceleration bearingless drive.

The paper analyzes the saturation effects occurring in two different drive claw types, and deduces an optimal drive claw design for the given requirements of high acceleration motors with large air gaps. The configuration of the motor and the classical T- and L-shaped drive claws are introduced in section II. Saturation effects in these drive claws are investigated by means of 3D finite element simulation and their impact on the motor torque is presented in section III. From these investigations a design procedure for an optimal drive claw based on the B2M concept is developed in section IV. The experimental verification of the 3D simulations and the design procedure are summarized in section V.

II. CONFIGURATION

The investigations presented in this paper are based exemplarily on the Bearingless 2-Level Motor (B2M) concept [4]. Briefly, the basic principle of this concept is the axial and circumferential separation of the bearing and drive windings, giving the motor the advantage of greatly reduced control effort as compared to [2] and significantly higher torque as compared to [1].

A homopolar magnetic bearing is implemented on the upper level, consisting of rotor and stator force biasing magnets and the bearing windings around the four stator claws. The rotor is levitated and kept in the centre position by means of controlled currents in the bearing windings causing attractive or repellent forces onto the rotor, respectively.

The axially lower level of the motor is reserved for the permanent magnet synchronous drive consisting of the round-shaped and diametrically magnetized rotor magnets with alternating polarisation direction and the drive claws with concentrated windings. With focus on a compact setup, the drive claws are additionally located between the bearing claws of the stator, since this greatly reduces the total height of the system. The 2-Level nature of the B2M concept allows the separate optimization of the bearing and the drive and also a clear analysis of the saturation effects in the drive claws. More details on the B2M concept are not presented here for the sake of brevity, but

the interested reader is referred to [4].

The following investigations focus on possible saturation effects in the drive claws, whereby two basic and well-known drive claw shapes, the T- and L-shape as depicted in Fig. 2, are considered and their applicability will be briefly discussed in the subsequent paragraphs.

The T-shaped drive claw as depicted in Fig. 2a is commonly used in standard ac drives [7]. It consists of the back iron, the pole shoes, where the drive windings are sitting, and the expanded pole shoe tip, which maximizes the coil flux-linkage. It provides a high phase inductance and a more sinusoidal torque characteristic [8]. In standard drives the distance between two pole shoe tips d_{Claw} is considerably larger than the magnetic air gap δ_{Mag} [9]. Therefore, the magnetic resistance of the air gap $R_{M,\delta}$ is consequently smaller than the magnetic resistance of the pole shoe tip gap $R_{M,T}$, making the flux path through the pole shoes and the air gap more attractive for the current imposed drive flux Φ_D than through the pole shoe tip gap. However, for the introduced bearingless motors with large air gaps the ratio between d_{Claw} and δ_{Mag} decreases, such that Φ_D tends to shortcut over the pole shoe tip gap d_{Claw} . Hence, this drive claw shape may be less appropriate for the applications at hand.

A greatly simplified design is the L-shaped claw as depicted in Fig. 2b. Here, the expanded pole shoe tips are cut off and the actual pole shoe is expanded, leaving the distance between two pole shoes d_{Claw} larger than double the air gap δ_{Mag} . This design leaves the magnetic resistance of the air gap $R_{M,\delta}$ smaller than the magnetic resistance of the claw gap $R_{M,T}$, making this design more favourable for large air gap drives.

In the following, the saturation effects occurring in these drive claw types will be analyzed by means of 3D finite element simulation [10], with the aim to identify the more appropriate concept for high acceleration requirements and large air gaps.

III. ANALYSES OF SATURATION EFFECTS

The general considerations of the preceding section showed the tendency that the presented L-shaped drive claw

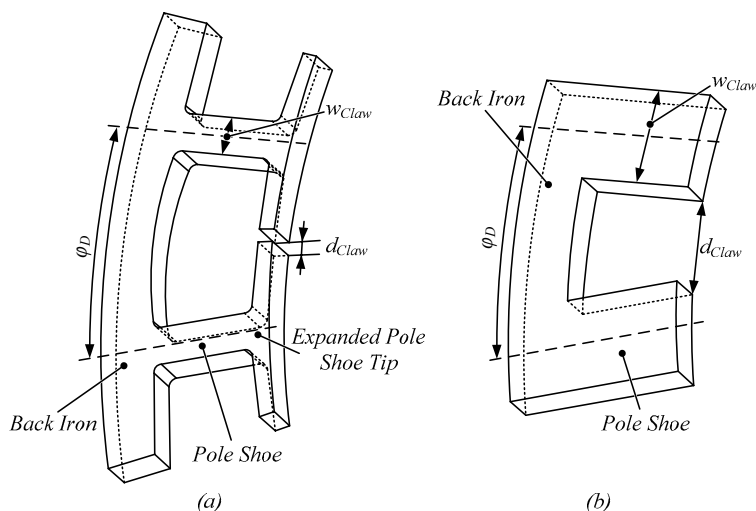


Fig. 2: Schematic view of (a) the T-shaped and (b) the L-shaped stator drive claw.

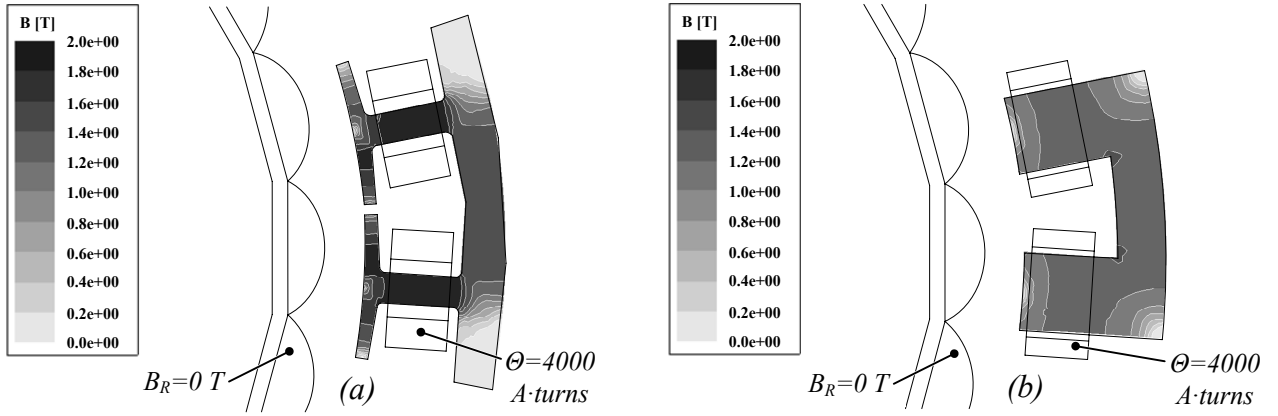


Fig. 3: Flux density distribution in a (a) T-shaped and in a (b) L-shaped drive claw caused by a magnetic voltage of $\Theta = 4000$ A·turns.

could be more appropriate for the application in bearingless motors with large air gaps than the presented T-shaped drive claw. The different applicability is possibly caused through different degrees of saturation in the drive claws, which will be reviewed by 3D finite element simulations using Maxwell® 3D [10] in this section.

Due to the nature of the permanent magnet synchronous machine there are two superimposed flux components in the drive claw, one being the flux imposed by the permanent magnets Φ_{PM} , and secondly the flux imposed by the drive winding current Φ_D . In order to visualize the interaction and the impact of the two flux components on each other the effects are considered separately in a first approach and are later merged together.

Basically, the magnetic saturation can be defined as a material property of a magnetic material that produces no significant change in magnetic flux density B for an increase of the magnetic field strength H , resulting in an air-like relative permeability ($\mu_r \approx 1$) [11]. In Fig. 3 the simulation results of the flux density distribution B within the drive claws caused by a magnetic voltage of $\Theta = 4000$ A·turns are depicted. The T-shaped drive claw in Fig. 3a shows a maximum flux density $B_{T,max}$ of 2 T at the pole shoes. Considering the saturation flux density of the claw material M-330A of $B_{Sat,M330A} = 1.4$ T, one

can see that the pole shoes are saturated, resulting in an air-like flux path through the claws. The saturation mainly arises from the small air gap d_{Claw} between the two pole shoe tips. The L-shaped drive claw in Fig. 3b also shows slight saturation, but the values of the flux density are generally much lower.

In the following, it shall be analysed, to which extent the presence of saturation in the drive claws (due to the impressed ampere-turns, cf. Fig. 3) influences the trajectories of the rotor flux. In particular, the amount of the flux Φ_{PM} that passes through the pole shoes is of interest, since this directly affects the motor torque M_D according to

$$M_D = \frac{U_{ind}(I_D, \varphi_R) \cdot I_D(\varphi_R)}{\omega_R} \quad (1)$$

with the induced voltage U_{ind} defined by

$$U_{ind} \sim \left. \frac{d\Phi_{PM}(I_D, \varphi_R)}{d\varphi_R} \right|_{I_D=const}, \quad (2)$$

the drive winding current I_D , the rotational angle φ_R and the rotational speed ω_R . Strictly, the employment of Eq. (1) and Eq. (2) for the torque calculation is only valid in case of no saturation, but they are presented to point out the general relationship between the variables.

For highlighting the effect of saturation a rotational angle

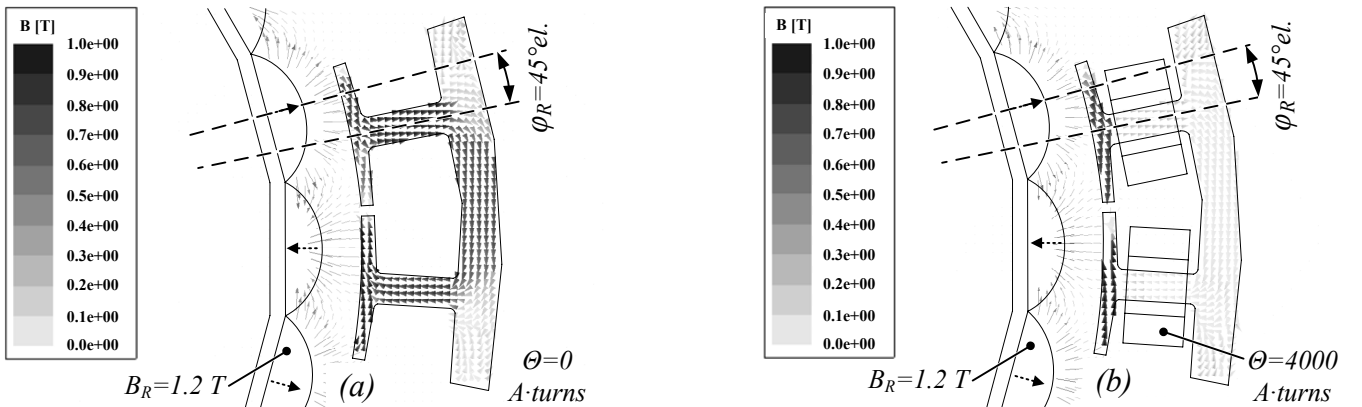


Fig. 4: Flux density distribution in a T-shaped drive claw caused by permanent magnets at a rotational angle of $\varphi_R = 45^\circ$ el. and a magnetic voltage of (a) $\Theta = 0$ A·turns and (b) $\Theta = 4000$ A·turns.

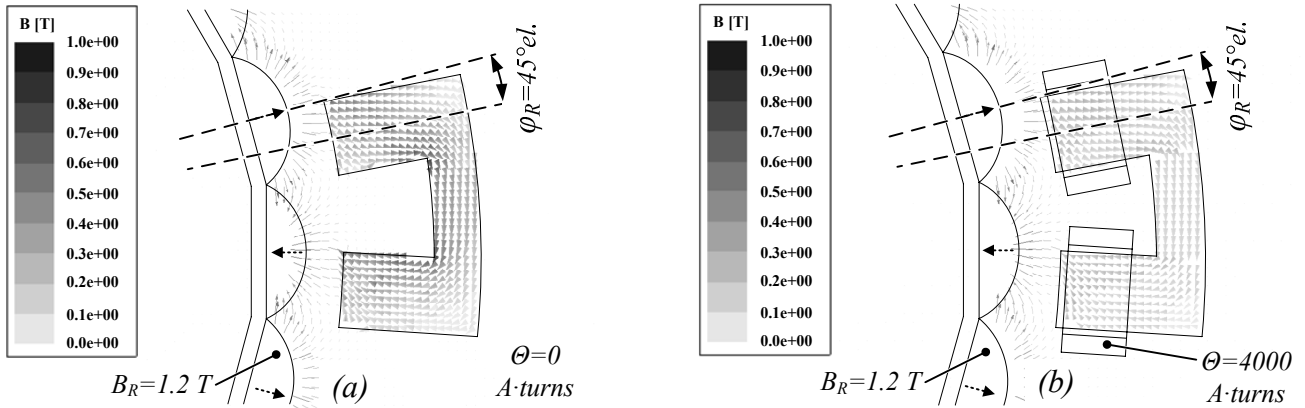


Fig. 5: Flux density distribution in a L-shaped drive claw caused by permanent magnets at a rotational angle of $\varphi_R = 45^\circ \text{el.}$ and a magnetic voltage of (a) $\Theta = 0$ A·turns and (b) $\Theta = 4000$ A·turns.

of $\varphi_R = 45^\circ \text{el.}$ between the permanent magnet poles and the drive claw pole has been chosen. Due to the field oriented control of the motor the phase angle $\varphi_{I,U}$ between the drive current I_D and the induced voltage U_{ind} is controlled to be zero [12]. Since U_{ind} is defined as the derivation of the flux Φ_{PM} with respect to the rotational angle φ_R (cf. Eq. 2), a phase angle $\varphi_{I,\Phi}$ of 90°el. between I_D and Φ_{PM} results. Therefore, zero drive current I_D and consequently no current imposed saturation appears at a rotational angle of $\varphi_R = 0^\circ \text{el.}$, while zero permanent magnet flux Φ_{PM} appears at a rotational angle of $\varphi_R = 90^\circ \text{el.}$, leaving $\varphi_R = 45^\circ \text{el.}$ as the optimal permanent magnet position to show the superposition of both effects.

In Fig. 4 and 5 the effect of claw saturation by a magnetic voltage of $\Theta = 4000$ A·turns on the permanent magnet flux trajectories through the drive claws is shown for both claw shapes by means of 3D simulation results. The comparison of Fig. 4a and 4b shows that the presence of saturation in the T-shaped claw makes the path through the pole shoes for the rotor flux less attractive. Therefore, the main flux part closes over the expanded pole shoe tips hardly entering the pole shoes. In comparison, the impact of the claw saturation on the L-shaped drive claw is shown in Fig. 5a and 5b. A slight reduction of the flux through the back iron is also visible for this drive claw, but the effect is clearly less distinct than for the T-shaped drive claw. Obviously, the smaller flux in the saturated T-shaped drive claw in Fig. 4b results in a significant reduction of the effective torque when compared to the L-shaped drive claw in Fig. 5b.

The introduced simulation results are based on an exemplary superposition of the drive winding current flux Φ_D and the permanent magnet flux Φ_{PM} , assuming a constant pre-saturation through certain level of ampere-turns and showing the level of saturation by the weakening of Φ_{PM} in the back iron. This is based on the assumption of a constant permanent magnet flux within the simulation environment. In reality, also the permanent magnet flux contributes to the flux density distribution and therefore influences the saturation of the drive claw. Furthermore, the resulting torque can not be exactly evaluated applying Eq. (1) due to the non-linear characteristic of the flux distribution. However, the results in Fig. 4 and Fig.

5 provide a good visualization of the saturation effects and a qualitative statement about the applicability of the claw shapes for high-acceleration drives with large air gaps.

The exact amount of torque reduction through claw saturation has to be evaluated by 3D simulations, which will be done in the subsequent sections in the course of the claw shape optimization. By all means, it can be stated that the L-shaped drive claw is more favourable for bearingless motors with large air gaps. Therefore, the next section presents an optimization procedure for the L-shaped drive claw.

IV. DESIGN OF OPTIMAL DRIVE CLAW

The preceding sections showed the negative influence of saturation effects onto the resulting motor torque. Since the introduced applications demand for a maximum possible torque, this specification can be reached by designing a drive claw using the whole available space along the stator perimeter (cf. Fig. 1), while having virtually no torque reduction through saturation effects in the whole operating range. The saturation investigations of section III showed a lower saturation affinity for the L-shaped drive claw shape, which will therefore be considered for the optimization procedure.

First, the stator claw opening angle φ_D is selected to 180°el. , since this maximizes the resulting torque characteristic, leaving w_{Claw} as the only mechanical parameter to be optimized (cf. Fig. 2b). Small values of w_{Claw} maximize the claw distance d_{Claw} and prevent magnetic shortcuts; however, such drive claws tend to saturation by the permanent magnet flux due to their small cross-section area and have a small coil flux linkage and consequently a small induced voltage. Very large values of w_{Claw} have to fit into the limited space and may result in a magnetic shortcut due to the reduced claw distance d_{Claw} , while having a big coil flux linkage. Considering the different torque limiting mechanisms for different stator claw widths a useful stator claw width range of $w_{Claw} = 10 \dots 35$ mm was applied for the parameter sweep for different ampere-turn ratios as depicted in Fig. 6, whereby each point represents a 3D simulation result. In Fig. 6 the small influence of w_{Claw} on the effective torque for w_{Claw} larger than 25 mm is visible. Apparently, the optimum stator width is in the range of 30 mm to 35 mm.

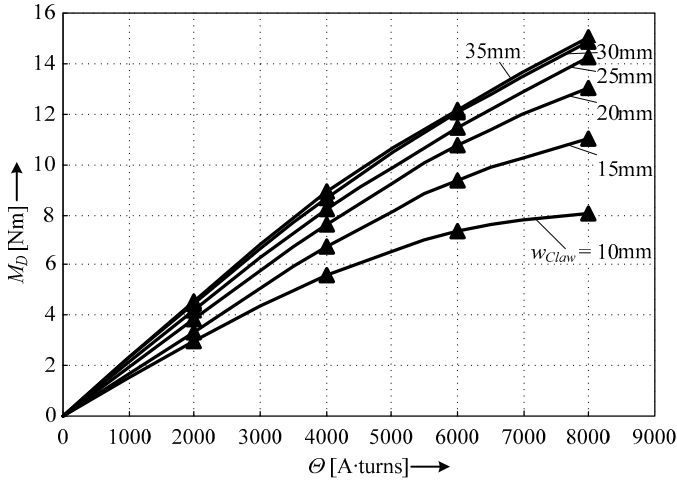


Fig. 6: Dependency of the initial motor torque M_D on the ampere turns, showing the impact of saturation effects for different drive claw widths w_{Claw} .

TABLE I

MAIN PARAMETERS OF PROTOTYPE

Outside Rotor Diameter D_O	410 mm (16.1 inch)
Mechanical Air Gap δ_{Mech}	7 mm (0.27 inch)
Number of Pole Pairs p	12
Motor Torque M_D per $\Theta = 1000$ A·turns	1.8 Nm
Rotor Mass m	5 kg (11 lbs)
Acceleration Time t_{acc} per Δn	1.9 s /1000 rpm
Circumferential Speed v_{Cr} @ $n = 2000$ rpm	155 km/h (96 mph)

However, also taking the negative influence of large values of w_{Claw} on the cogging torque into account [4], 25 mm is a very good selection and has therefore been considered for the experimental verification in the subsequent section.

V. EXPERIMENTAL VERIFICATION

A comparison between the 3D simulations and the experimental performance of the prototype depicted in Fig. 7 is presented in this section in order to prove the applicability of the before formulated optimal design guidelines. The main parameters of the prototype are summarized in Table I.

In order to show the influence of the drive claw saturation on the motors torque behaviour, the L- and T-shaped drive claws were manufactured and evaluated through acceleration tests. The most rugged and exact method is based on Eq. (3), where the motor torque M_D can be calculated through the acceleration time Δt_{acc} needed to accelerate a body with a known moment of inertia J over a certain rotational speed span Δn .

$$M_D = J \cdot \frac{2\pi}{60} \cdot \frac{\Delta n}{\Delta t_{acc}} \quad (3)$$

This equation is only valid in the linear region and is evolved for a constant current, not considering the current limiting properties of the drive windings inductance.

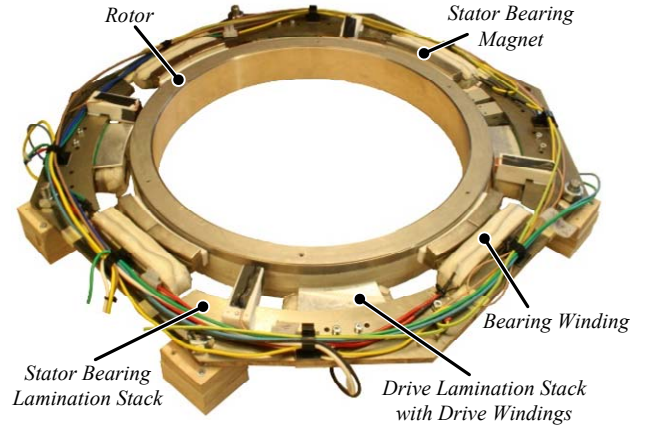


Fig. 7: Experimental Prototype of B2M.

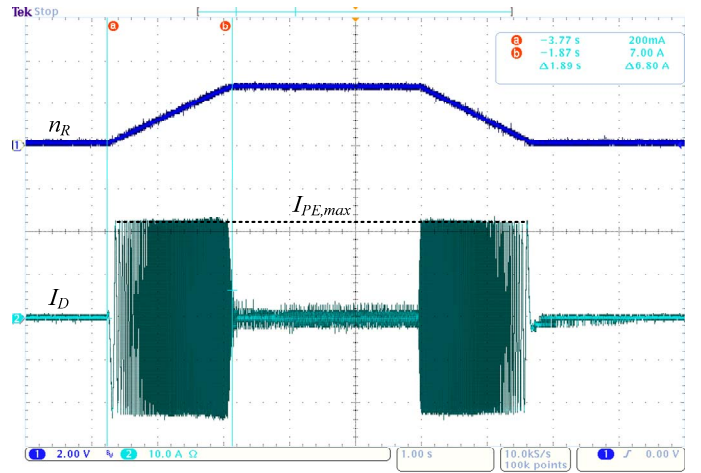


Fig. 8: Acceleration behaviour of B2M prototype from 0 to 1000 rpm for a maximum current limited by the power electronics to $I_{PE,max} = 22$ A (with the drive claw winding number $N_D = 300$, this results in a maximum ampere-ratio of $\Theta_{Peak} = 6600$ A·turns) in 1.9 s and deceleration in 1.5 s (scales: 800 rpm/div., 10 A/div., 1 s/div.).

Two alternative methods for the torque measurement could be employed too, but are associated with the higher efforts. First, the torque measurement with a rotational torque transducer requires an extra measurement setup, conflicting with the aim for a low constructional effort method. Second, a torque calculation method based on Eq. (1) demands the measurement of the induced voltage U_{ind} , which is not directly accessible. Adding a measurement coil results in noisy waveforms due to the inductively coupled and switched drive current I_D . Even a constant current presaturation does not lead to exact values due to the non-linearity of the investigated phenomena.

Hence, with the aid of the initially mentioned integrative measurement method based on the acceleration time, the motor torque performance of the prototype was investigated for the two different stator claw shapes. An exemplary oscilloscope screenshot showing the drive current I_D for an acceleration test from 0 to 1000 rpm is depicted in Fig. 8. A comparison of the 3D simulation results and the measurement data is depicted in

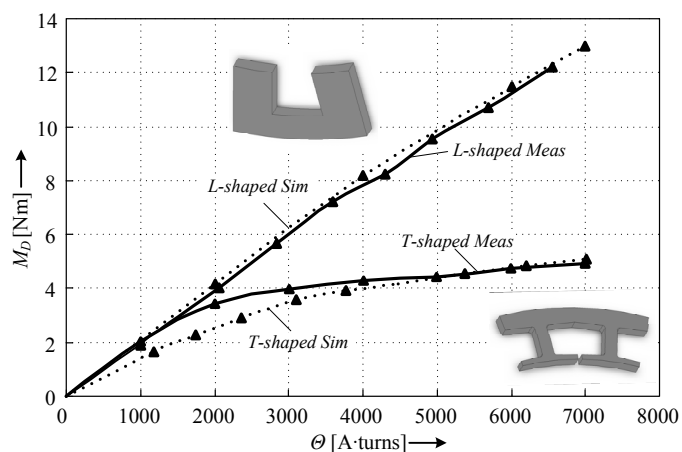


Fig. 9: Comparison of the experimental performance and the 3D simulation results for the B2M prototype for different stator drive claw shapes.

Fig. 9, which illustrates the superior performance of the optimized L-shaped drive claw ($w_{Claw} = 25\text{mm}$), which features a nearly linear torque increase over a wide range of peak ampere-turns θ_{Peak} , while the T-shaped claw shows significantly lower torque values due to the investigated saturation effects. Both simulated curves show a good match with the experimentally determined data, verifying the 3D simulation as a fast and reliably optimization and visualization tool for the given task.

VI. CONCLUSION

In this paper the impact of saturation effects on the effective torque of bearingless motors with large air gaps was investigated. For this purpose, the applicability of two commonly known drive claw shapes (T- and L-shaped drive claw) in the exemplary “Bearingless 2-Level Motor (B2M)” was evaluated by general magnetic flux path related considerations and subsequently by means of 3D finite element simulations. The influence of the saturation effects on the relevant torque-generating flux components was illustrated by simulation

model based plots of the flux density distribution, resulting in the selection of the L-shaped drive claw as the geometry of choice. In a following optimization of the L-shaped drive claw the claw width was selected, considering the limited space issue of the concentrated windings, the different mechanisms of saturation and the cogging torque. The experimental verification on a laboratory prototype of the B2M showed a good match of the simulation results and measurement data and highlights the superior and nearly linear torque behaviour of the L-shaped drive claw in the whole operating range.

REFERENCES

- [1] T. Schneeberger, J. W. Kolar, “Novel Integrated Bearingless Hollow-Shaft Drive,” *Proc. of the IEEE Ind. Applic. Conf. IAS*, Tampa (USA), 8–12 Oct. 2006.
- [2] W. Gruber, W. Amrhein, “Design of a Bearingless Segment Motor,” *Proc. of the 10th Int. Symp. on Magnetic Bearings*, Martigny, 2006.
- [3] R. Schoeb, N. Barletta, “Principle and Application of a Bearingless Slice Motor,” *JSME Int. Journal Series C*, pp. 593-598, 1997.
- [4] P. Karutz, T. Nussbaumer, W. Gruber, J.W.Kolar, “The Bearingless 2-Level Motor,” *Proc. of the 7th Int. Conf. on Power Electronics and Drive Systems*, Bangkok, Thailand, Dec. 2007.
- [5] J.-P. Yonnet, “Permanent magnet bearings and couplings,” *IEEE Transactions on Magnetics*, vol.17, no.1, pp. 1169-1173, Jan. 1981.
- [6] M. Nakagawa et al., “Optimization of Stator Design in a Consequent-Pole Type Bearingless Motor Considering Magnetic Suspension Characteristics,” *IEEE Transactions on Magnetics*, vol.42, no.10, pp. 3422-3424, Oct. 2006.
- [7] H.-P. Nee, “Rotor slot design of inverter-fed induction motors,” *Seventh International Conference on Electrical Machines and Drives*, no. 412, pp.52-56, 11-13 Sep 1995.
- [8] Y. Pang, Z.Q. Zhu, D. Howe, “Analytical determination of optimal split ratio for permanent magnet brushless motors,” *IEE Proc. of Power Applications*, vol. 153, no. 1, pp. 7-13, Jan. 2006.
- [9] A. Chiba, T. Fukao, O. Ichikawa, M. Oshima, M. Takemoto, D. Dorrell, “Magnetic Bearings and Bearingless Drives,” 1st edition, Newnes, pp. 368–377, May 2005.
- [10] Maxwell® 3D by Ansoft Corporation, <http://www.ansoft.com>.
- [11] R.W. Erickson, D. Maksimovic, “Fundamentals of Power Electronics,” 2nd Edition, New York, Springer, pp. 493-495, 2001.
- [12] C. Schauder, “Adaptive speed identification for vector control of induction motors without rotational transducers,” *IEEE Transactions on Industry Applications*, vol.28, no.5, pp.1054-1061, Sep/Oct 1992.